Applied Thermal Engineering 263 (2025) 125332

Contents lists available at ScienceDirect

Applied Thermal Engineering

journal homepage: www.elsevier.com/locate/apthermeng

Research Paper

A numerical framework for 3D Computational Fluid Dynamics (CFD) simulations of gasoline-fuelled burners to be adopted in catalyst preheating of vehicle exhaust systems

Stefano Sfriso [a,*], Fabio Berni [a], Stefano Fontanesi [a], Stefano Paltrinieri [b], Fabio Santi Mortellaro [b], Vincenzo Rossi [b], Luca Brocchi [b], Roberto Tonelli [b], Massimo Medda [b]

[a] Università degli studi di Modena e Reggio Emilia, Italy
[b] Ferrari S.p.A, Italy

A B S T R A C T

Air pollution from vehicular traffic is a growing concern, leading to stricter regulations on the exhaust gas emissions. In case of spark-ignition gasoline engines, the limitation of the emissions is challenging, especially during the cold start, when the already critical conditions combine with the inefficiency of the aftertreatment system because of the low temperature. A possible solution to reduce the light-off time needed to bring the catalyst to the operating temperature is represented by a gasoline-fuelled burner, which produces and drives the hot exhaust gases towards the aftertreatment system. This strategy is useful not only for traditional oil-derived gasoline, but also for carbon neutral fuels such as e- and bio-gasoline. In the present paper, a 3D-CFD modelling framework for the simulation of gasoline-fuelled burners for catalyst preheating is proposed and validated against experimental data on a prototype. The framework is mostly inherited from in-cylinder simulations of spark-ignition internal combustion engines, in order to demonstrate that a unique numerical setup can be exploited for multiple purposes with undoubtful saving of cost and time. In this regard, two well consolidated combustion models for engine simulations are tested, namely ECFM-3Z and Detailed Chemistry (DC). Alternative spray and liquid film stripping models are purposely developed in this work and presented in the paper. Validation is carried out by comparing numerical temperature and emissions at the exhaust of the burner with the experimental counterparts. Both the combustion models are able to properly match the experimental outlet temperature, with an error lower than 4 %. As for the emissions, ECFM-3Z and DC are able to predict, at least as order of magnitude, the ppm concentrations of NO and CO at the exhaust. Overall, a good agreement is obtained between simulations and experiments with both the models.

Besides the proposal of a robust 3D numerical framework, the present paper aims at demonstrating the primary role of the CFD to evaluate and understand phenomena that cannot be easily investigated via experiments. In fact, prefilmer effectiveness and wall heat losses are identified by the simulations as the most critical aspects of the prototype. In particular, prefilmer and adiabatic efficiencies result equal to 78.2 % and 73.1 %, respectively. These values lead to a poor global efficiency of the burner, equal to 56.1 %, despite a combustion efficiency of 98.2 %. Finally, the combustion regime inside the investigated burner is analysed and the adopted combustion models are found to be (partly or totally) out of their applicability range. Nonetheless, similarly to in-cylinder simulations, they are still capable to provide promising results if properly tuned, as confirmed by the presented validation. The proposed numerical framework is fuel-agnostic, i.e. it can be applied to conventional, e- and bio-gasoline like fuels.

1. Introduction

The recent Euro 7 legislation has not tightened further the limits on the exhaust gas emissions coming from passenger cars powered by internal combustion engines (ICEs). Nonetheless, tailpipe emissions still remain a challenge for car manufacturers. Furthermore, despite the recent EU regulation which sets the target of 0 g/km of CO_2 starting from 2035 [1] (with "excess emissions premium" in case of overcoming), EU itself has opened the way to carbon neutral fuels in the same regulation. In other words, passenger cars fuelled with bio- or e-gasoline after 2035 may not be a myth. Therefore, in this scenario, the reduction of pollutant emissions is expected to stay as a hot topic also in the future.

Recently, design efforts to comply with the standards have been increasingly focused on the reduction of cold start emissions. This requires the shortening of the time needed for the catalyst to reach the light-off temperature.

In literature, some authors addressed such goal through engine management strategies [2], with good performance in terms of catalyst light-off time reduction, but at the expense of high fuel penalties caused by heat losses and unburnt fuel.

As an alternative, electric heaters were extensively investigated to

* Corresponding author.
E-mail address: stefano.sfriso@unimore.it (S. Sfriso).

https://doi.org/10.1016/j.applthermaleng.2024.125332
Received 31 July 2024; Received in revised form 22 November 2024; Accepted 23 December 2024
Available online 26 December 2024

Nomenclature

A	Constant for chemical time scale computation
A_{geom}	Geometrical area
A_w	Bai-ONERA calibration constant
α	Spray cone angle
c_a	Contraction area coefficient
CAD	Computer Aided Design
c_f	Bai-ONERA calibration constant
CFD	Computational Fluid Dynamics
D	Pipe diameter
d	Droplet diameter
Da	Damkohler number
DC	Detailed Chemistry
D_e	External diameter
Da_{fl}	Flame Damkohler number
D_i	Internal diameter
Da_{ext}	Flame Damkohler number at upper limit of diffusive flame extinction
Da_{lfa}	Flame Damkohler number at lower limit of diffusive flamelet combustion
Da_{se}	Damkohler number at which a steady laminar stagnation point flame extinguishes
D_n	Nozzle diameter
DNS	Direct Numerical Simulation
δ	Laminar flame thickness
δ_x	Local boundary layer thickness
d_0	Reference droplet diameter
E	Stripped to liquid film mass ratio
ECFM-3Z	Extended Coherent Flamelet Model 3 Zones
η_{ad}	Adiabatic efficiency
$\eta_{internal}$	Internal efficiency
η_{comb}	Combustion efficiency
$\eta_{prefilmer}$	Prefilmer efficiency
η_{tot}	Burner (i.e. total) efficiency
η_t	Kolmogorov turbulence length scale
EU	European Union
GDI	Gasoline Direct Injection
h	Liquid film height
HR	Heat Released
HRR	Heat Release Rate
HT	Heat Transfer
ICE	Internal Combustion Engine
Ka	Karlovitz number
L	Liquid film spreading length before stripping edge
LHV	Lower Heating Value
l_t	Turbulent length scale
$\dot{m}_{inj}$	Fuel injected mass flow rate
m_{inj}	Fuel injected mass
m_{film}	Liquid film mass
$\dot{m}_{film}$	Liquid film mass flow rate
$\dot{m}_{strip}$	Stripped liquid film mass flow rate
μ_g	Gas dynamic viscosity
N	Number of droplets
n	Bai-ONERA calibration constant
ν	Kinematic viscosity
PDA	Phase Doppler Anemometry
PHEV	Plug-in Hybrid Electric Vehicle
PISO	Pressure-Implicit with Splitting of Operators
q	Rosin-Rammler distribution exponent
RANS	Reynolds-Averaged Navier-Stokes
RCCI	Reactivity Controlled Compression Ignition
r_{ds}	Bai-ONERA calibration constant
Re_t	Turbulent Reynolds number
Re_x	Reynolds number, $\frac{\rho_g u_g \delta_x}{\mu_g}$
ρ	Density
ρ_g	Gas density
ρ_l	Liquid density
SI	Spark-Ignition
S_l	Laminar flame speed
SMD	Sauter Mean Diameter
σ	Surface tension
Ta	Constant for chemical time scale computation
$\widetilde{T}_b$	Favre-averaged cell burnt temperature
τ_c	Chemistry time scale
ts	Time step
u'	Turbulent fluctuation
u_g	Gas velocity
U_{mean}	Mean velocity
v	Droplet velocity
v_{eff}	Effective velocity
v_l	Velocity of liquid film
V_l	Liquid volume fraction
VOF	Volume Of Fluid
v_t	Droplet tangential velocity
w	Liquid film width
We_g	Gaseous Weber number
We_x	Weber number, $\frac{\rho_g \delta_x {u_g}^2}{\sigma}$
Y	Probability of occurrence of a certain diameter in the Rosin-Rammler distribution

preheat the catalyst before engine start, with promising results in the emission reduction. For example, Bargman et al. [3] developed and tested an electrically preheated catalyst for PHEV vehicles, while Mianzarasvand [4] performed a CFD sensitivity study on an electrically preheated catalyst for motorcycles. Canè [5] proposed a strategy in which the electric preheating of the catalyst in a diesel plug-in vehicle is planned thanks to a prediction of the first engine start by vehicular connectivity. Hofstetter [6] developed a management strategy combining the use of thermal engine, electric motor and catalyst electric heater for the reduction of the cold start emissions in a hybrid diesel vehicle. In addition, Gao [7] and Garcìa [8] have demonstrated the effectiveness of the electrically heated catalyst on diesel and RCCI gasoline-diesel engines, respectively.

A further approach for the catalyst preheating provides for the adoption of a fuel burner. Such a solution is not a novelty as demonstrated by the works of Hepburn [9] and Zu Schweinsberg [10]. However, the interest on this technology has revamped in the last years. Recently, Rossi et al. [11] proposed the adoption of a gasoline-fuelled swirling burner to preheat the catalyst in high-performance spark-ignition (SI) engines. This approach could potentially increase the overall system efficiency by extracting heat directly from gasoline, rather than converting gasoline into mechanical power, then into electric energy and, finally, into heat again. Furthermore, the heat flux achieved by this method is potentially higher, reducing the time required to reach the catalyst operating temperature. Battistoni et al. [12] proposed the design of a burner for SI engines by means of combined simulations and experiments.

Focusing on fuel burners for light-off time reduction in SI engines, the development of a valid design is far from being trivial. It has to be characterized by nearly "0" emissions, not to increase those from the engine exhaust. This can be a critical issue. In fact, considering the low injection pressure (as the fuel is usually not supplied by the rail of the

GDI system) and thus a limited droplet break-up, the risk of liquid film formation and/or poor mixing is high, leading to non-negligible concentrations of emissions (in primis unburnt hydrocarbons) at the exhaust. In order to facilitate the design and reduce the cost-to-market, 3D-CFD can be proficiently adopted. For example, it can be exploited to optimize geometry and strategies (such as the injection one) or even deepen aspects that cannot be easily investigated by experiments. In this regard, the present work proposes a 3D-CFD framework to simulate combustion inside gasoline fuelled burners to be adopted in the exhaust line of SI engines for light-off time reduction. It relies on approaches for injection and liquid film stripping that are purposely developed for the present work. The rest of the setup is well consolidated in engine simulations, in fact it is inherited from in-cylinder analyses. This is important, since the possibility to extend the use of a numerical framework to the study of a different device means simplification and saving of both cost and time. In particular, two extensively validated combustion models for SI engines (namely ECFM-3Z and DC) are utilized and compared.

With respect to the (very sparse) existing literature dealing with gasoline burners for catalyst preheating, the present work represents a novelty for different reasons. First of all, alternative models for spray and liquid film stripping are purposely developed. Secondly, compared to [12] where only Detailed Chemistry is adopted, in the present paper both DC and a flamelet model (namely ECFM-3Z) are effectively adopted. Thirdly, a quantitative validation of the proposed numerical framework is here presented, showing a reasonable agreement of the numerical outcomes with the experiments. Moreover, the combustion regime inside the burner is deeply analysed to assess, from a theoretical point of view, the applicability of DC and ECFM-3Z, which are suitable for well stirred reactor and flamelet regimes, respectively. Finally, this work aims at emphasizing the potential of CFD. In fact, thanks to the numerical results, the efficiency of the burner is calculated, the gaps of the proposed prototype are highlighted and guidelines for future design improvements are proposed.

It is important to point out that the proposed validation takes place against experimental data on a very preliminary prototype, for which there are less confidentiality restrictions in terms of data disclosure. Nonetheless, the validity of the proposed methodology is not affected as it is effective regardless the specific geometry.

After a brief description of the experimental conditions and facilities, the 3D-CFD framework is presented, with particular focus on the purposely developed models. Specifically, spray and liquid film stripping models are accurately introduced, as they are crucial for a proper prediction of fuel evaporation and mixing and, thus, of the heat release rate. Then, the validation with respect to the experiments is proposed. Results in terms of exhaust gas temperature and emissions provided by both the tested combustion models are compared to the experimental outcomes. After the validation, CFD outcomes are deeply analysed in terms of burner efficiency, combustion mode and combustion regime. Finally, conclusions are drawn.

2. Experimental tests

Fig. 1 schematically illustrates the structure of the burner. The surrounding components are reported as well. As visible, there are an air pump used to push air through the burner and a hollow cone swirling injector to introduce gasoline.

Fig. 2 shows the 3D CAD model of the exhaust line with the burner. Interestingly, the exhaust manifold is specifically designed and optimized to mix the streams coming from engine and burner. The latter turns on few seconds before the engine start, so that the aftertreatment system reaches the required temperature promptly [13].

In the experimental tests considered for the present paper, the whole aftertreatment system (from the manifold and on) is removed and replaced by a long straight pipe where emissions are sampled. Moreover, the exhaust gas from the engine is not present. The burner is made of three main modules: swirler (with a prefilmer), combustion chamber and exhaust pipe. The modular design of the burner assembly makes it flexible for geometrical variations (i.e. each single module can be replaced to test alternative solutions). The swirler component is bladed and specifically designed to generate a highly turbulent swirling flow to enhance fuel–air mixing and accelerate combustion. However, it is important to carefully balance the air flow rate to prevent fuel vapor from being dragged away from the spark plug before it has a chance to ignite. Similarly, excessively high air velocity between the spark plug electrodes can lead to misfires. These challenges are addressed through the use of appropriate air mass flow and injection timing strategies. As for the prefilmer, it has not to be intended as in traditional applications, where a liquid is slipped on a surface and then strips thanks to the air flow. In this case, the liquid is present because of the formation of film as a consequence of the fuel spray impingement. In other words, fuel is injected towards the prefilmer to form film which should then strip under the action of the air flow. This is sought, instead of direct injection into the chamber, to promote spray break-up (and, hence, evaporation) as the injection pressure is extremely low. The prefilmer is characterized by a very simple shape as it is a cylinder with reduced diameter (connecting swirler and combustion chamber) to increase the probability of spray impact on the wall. A schematic representation of the prefilmer is reported in Fig. 3.

In the test rig, multiple probes are installed. Besides pressure sensors,

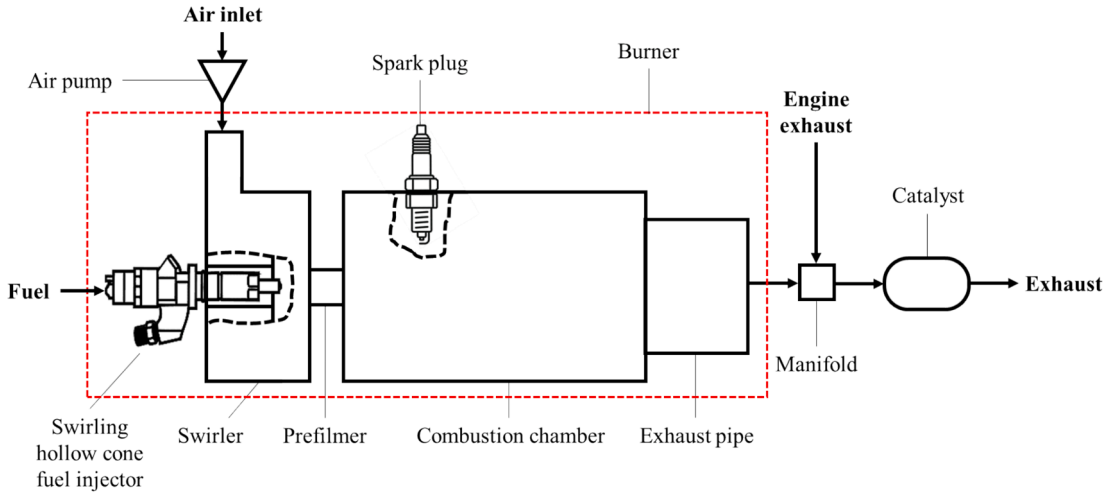

Fig. 1. Schematic representation (not in scale) of burner (indicated by the red box) and exhaust line layout.

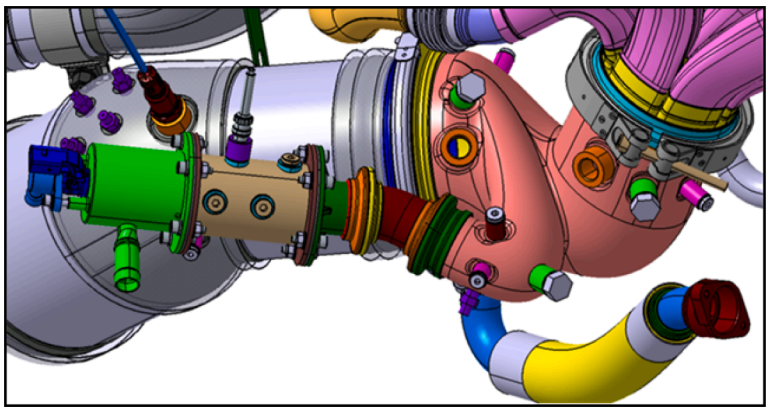

Fig. 2. 3D CAD model of the exhaust line with burner.

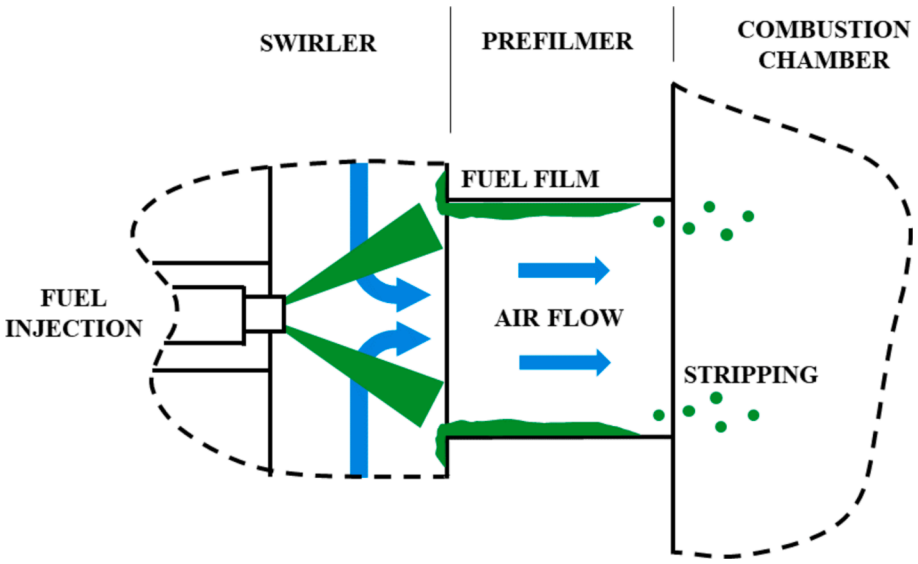

Fig. 3. Schematic representation of the prefilmer operation.

thermocouples are placed at the outlet pipe, to monitor the temperature of the hot gases. In detail, K type thermocouples are adopted, with accuracy of ±0.75 %. A lambda sensor is mounted in the manifold to check the equivalence ratio. Emissions are measured by the instruments exhaustively described in [11], where accuracies are reported as well. Injection pressure and frequency are equal to 5 bar and 100 Hz. The air mass flow rate ($\dot{m}_{air}$) is constant and equal to 30 kg/h during the steady state operation. The inlet temperature of the air is set to +30 °C. The combination of injection characteristics and air mass flow rate leads to an equivalence ratio $\varphi = 0.9$ (on average). As for the ignition, a spark plug located in the combustion chamber is excited by a 200 Hz signal. The experiments point out that, during the steady-state operation of the burner, the ignition can be cut off without altering the efficiency of the device. In the present paper, only the steady-state operation of the burner is considered for the numerical analyses.

3. 3D-CFD FRAMEWORK

As previously anticipated, one of the most interesting aspects of the proposed 3D-CFD framework is that it is mostly inherited by in-cylinder simulations. All the adopted models (such as turbulence and combustion ones) are well consolidated in the literature for SI ICEs. The only exceptions deal with specific aspects. In particular, spray and liquid film stripping are investigated by purposely developed approaches which will be described in the following.

3.1. General setup and combustion modeling

The simulations are carried out using STAR-CD, licensed by SIEMENS DISW. The PISO algorithm is adopted for pressure–velocity coupling. A RANS approach to turbulence is preferred, with a high-Reynolds wall treatment. The k-ε RNG [14,15] turbulence model is selected as already employed by the authors in previous engine simulations [16–20]. The Improved GruMo-UniMore model, available in STAR-CD, predicts the wall heat fluxes as it is widely validated [21–23] at engine-like conditions. It accounts for the actual Prandtl number of the mixture and it is able to compute the heat transfer accurately regardless the near-wall grid resolution. The differencing scheme adopted for the scalar transport equations is MARS [15]. As for the scalar properties, they are represented by temperature-dependent polynomials. The ideal gas law is used to close the set of equations. The numerical grid is made of hexahedral cells with a characteristic size of 2 mm. Local refinements are present (for example in correspondence of the prefilmer), with a cell size down to 0.25 mm. The total number of cells is nearly 540 k. The timestep is chosen equal to 1.67×10^{-5} s during the entire simulation. As for the domain, besides the burner, the straight pipe where emissions are sampled is included (at least up to the section where the experimental probes are placed, which is located roughly 0.5 m downstream the burner).

Two different combustion models are tested, namely ECFM-3Z [15] and pure DC [15]. ECFM 3Z is a flamelet model widely adopted in ICEs,

where the flamelet regime is the most common one. It separates chemistry and turbulence contributions on the flame propagation. Briefly, the turbulent flame is modeled as a laminar one (in terms of structure) wrinkled by turbulence. By the transport of a flame surface density, ECFM-3Z accounts for the turbulent wrinkling of the flame, while the chemistry influence is resumed in the laminar flame speed. For the simulation proposed in the present paper, the laminar flame speed is computed via the definition of a surrogate fuel (mimicking the actual gasoline) and 1D chemical kinetics simulations. Details can be found in references [24] and [25]. For the premixed mode, ECFM-3Z relies on a one-step reaction [26] which provides for $C_{7.3}H_{13.2}$ as a fuel (well representative of a commercial gasoline) and CO among the products. Thanks to the double conditioning of the computational cell, ECFM-3Z is also able to identify the fuel evaporating behind the flame front. Therefore, it can model diffusive combustion as well. For this mode, the eddy break-up assumption is used to calculate the fuel burning rate [15]. From a chemical standpoint, behind the flame (i.e. in the burnt gases), a 4-step oxidation mechanism [15,27] is implemented, which provides for formation of CO other than the complete combustion products (CO_2 and H_2O). Still in the burnt region, the NO chemistry is implemented. In particular, the classical extended 3-step Zel'dovich mechanism [15] is solved to obtain the NO concentration in each computational cell.

As for the DC, the turbulence-flame interaction is not accounted for. The transport equations of all the reacting species are solved introducing a detailed multi-step chemical reaction mechanism as a source term. Therefore, in a RANS framework, DC should be exploited just in case of "well-stirred reactor" combustion regime, that is, for example, in case of very reduced reaction rates. However, following a common practice for ICEs, DC is exploited also for the flamelet regime and the turbulence-flame interaction is accounted for by ad-hoc tuning of diffusion. De facto, the turbulence effect becomes a calibration parameter rather than a modeling effort. The default setting of the DC model implemented in STAR-CD is characterized by a scaling factor equal to 1.7 that multiplies both the diffusive term in the transport equations of enthalpy and scalars and the source term (i.e. the production rate governed by the chemical kinetics scheme) in the scalar transport equations. In this regard, in the present work, both ECFM-3Z and DC are employed with the default settings (i.e. default calibration constants). With the detailed chemistry approach, in order to save computational cost and, simultaneously, simplify the research of a chemical mechanism, a single component fuel is considered instead of the actual gasoline and C_8H_{18} is selected for the purpose. The reduced chemical mechanism [28] adopted in the present paper contains 109 species, 543 reactions and paths for both *iso*-octane oxidation and NO_x formation. Therefore, by means of the selected scheme, CO and NO concentrations can be predicted to be compared with the experimental data.

In this work, the attention is mainly focused on the steady-state operation of the burner, when the spark-plug can be switched off. For this reason, the ignition modeling is simplified. In particular, for both the models, no time delay between nominal spark time and kernel deposition is introduced. Moreover, ignition occurs by the deposition of a spherical kernel with radius of 1 mm. In ECFM-3Z, the kernel is made of burnt mass while, in DC, it is a volume characterized by unburnt temperature equal to 2500 K. The reason for a simplified approach to ignition is justified considering that, firstly, the burner starting phase is not investigated in the present work (in fact, the achievement of the steady-state operation is sped up by a proper initialization of the domain). Secondly, as it will be commented in the result section, ignition is switched off during the steady operation in both simulations and experiments, to demonstrate that the device (as well as its numerical model) can properly work without spark assistance.

3.2. Spray modeling (with validation)

Inside the burner, the gasoline spray is treated by a lagrangian approach. Therefore, the burner simulations rely on a combined eulerian–lagrangian framework. In order to reproduce the primary break-up process without detailed modelling, parcels are injected with a pre-computed speed and a diameter following the Rosin-Rammler (RR) distribution reported in Eq. (1).

$$Y = 1 - e^{-\left(\frac{d}{d_0}\right)^q} \tag{1}$$

Y is the mass fraction of droplets with diameter less than d, d_0 is the characteristic particle size and q a parameter which governs the width of the distribution. In order to obtain the initial velocity of the parcels and the parameters of the RR, a multiphase simulation of the internal nozzle flow is carried out in STAR-CCM+, licensed by SIEMENS DISW. The simulation is unsteady and based on RANS equations. Usually, in this type of simulations, besides the internal nozzle geometry, a portion of the outer domain is included. In this case, in order to speed up the simulation, only the injector geometry is considered, that means the outlet boundary coincides with the nozzle outlet. In this way, it is possible to reduce the computational effort. The needle is placed in a fixed position corresponding to the maximum lift, to simulate the steady-state operation of the injector. In order to account for the multiple phases, the Volume of Fluids (VOF) method is employed. The utilized fuel is a single-component mimicking the actual gasoline and it is the same used for the burner simulations. The k-ω SST turbulence model is preferred along with a low Reynolds wall treatment. Fig. 4 shows the liquid phase volume fraction at the nozzle outlet resulting by the simulation. It is then possible to compute the contraction area coefficient (c_a) as the ratio between liquid volume fraction (V_l) surface integral and geometric area (A_{geom}) of the nozzle hole, as in Eq. (2).

$$c_a = \frac{\int_{A_{geom}} V_l dA}{A_{geom}} \tag{2}$$

The contraction area coefficient c_a is used to determine the diameter of the droplets exiting the nozzle, computed as the thickness of the circular crown formed by the fluid at the injector outlet visible in Fig. 4.

More in detail, Eq. (3) provides D_i, which is the internal diameter of the crown, while D_e is known as it corresponds to the injector hole diameter.

$$\frac{\pi}{4} D_e^2 c_a = \frac{\pi}{4}\left(D_e^2 - D_i^2\right) \tag{3}$$

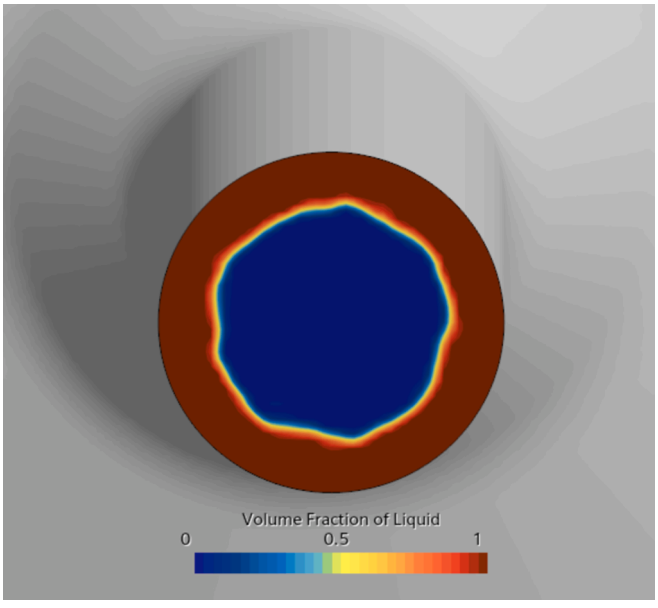

Fig. 4. Liquid phase volume fraction at the nozzle outlet.

Then, the droplet initial diameter is defined as in Eq. (4).

$$d_0 = \frac{D_e - D_i}{2} = \frac{D_n}{2}\left(1 - \sqrt{1 - c_a}\right) = 60\mu m \quad (4)$$

D_n is the nozzle diameter which coincides with the outer diameter of the crown (D_e). d_0 value is used as the center of the Rosin-Rammler distribution for the initial droplet diameter.

In order to compute the initial velocity of the droplets, the mass flow averaged velocity magnitude is calculated at the nozzle exit. With the injector feeding pressure set to 5 bar, the injected droplets attain an effective velocity of nearly 20 m/s.

As for the outer cone angle of the spray, the direction of the velocity vectors at the outlet of the injector is considered. Since the latter is swirling, the resulting vectors are those reported in Fig. 5a), where velocity magnitude at the outlet and streamlines are visible as well. Firstly, in the core region, the flow is directed inward. Secondly, unlike the radial components that are almost null, the tangential ones of the velocity vectors are not negligible. Such a vector distribution is responsible for the spray opening as well as for the formation of a hollow cone spray. For a quantitative estimation of the outer cone angle, a cylindrical coordinate system is considered at the nozzle exit, as visible in Fig. 5b). Then, the mass flow averaged tangential component of the velocity at the injector outlet (v_t) is computed. Thanks to v (previously calculated and equal to 20 m/s) and v_t (both supposed as applied in correspondence of the injector axis), the average direction of the liquid exiting through the hole is obtained and it is given by α. α is nearly 40° and it is adopted as semi-cone angle.

Since the resulting spray is hollow cone, the inner semi-cone angle has to be determined. This parameter along with q of the Rosin-Rammler distribution are purposely calibrated to match the experimental data. In particular, they are chosen equal to 20° and 2.5, respectively.

Moving to the secondary break-up, the Reitz-Diwakar model [29] is chosen with the constants proposed in Table 1. The values shown in the table are different from the default ones; in fact, a calibration of the model is needed as a consequence of the very low injection pressure.

To calibrate the lagrangian model of the spray (in particular the secondary break-up constants) before the adoption in the burner, a dedicated unsteady simulation is carried out in STAR-CD. Specifically, the spray is tested in a quiescent vessel and the validation is performed against experimental data in terms of liquid penetration, phase doppler anemometry (PDA) and imaging.

The initial conditions for the droplets (in terms of size and velocity) as well as the secondary break-up are the ones proposed above. As for the vessel, initial pressure and temperature are equal to ambient conditions. The rest of the setup (i.e. numerics, turbulence model, etc.) of the simulation is the same adopted for the burner investigation, in order to keep the behaviour of the spray unchanged between vessel and burner.

Table 1
Reitz-Diwakar model calibration constants.

We (bag)	3.6
We (stripping)	0.03
Te (bag)	3.14159
Te (stripping)	47

Fig. 6 shows the comparison between computed and experimental liquid penetrations during the injection process, with a strong agreement between the two. As a further validation, numerical diameters and velocities of the droplets are compared to the experimental counterparts. In particular, the comparison takes place at the points shown in Fig. 7, which are placed 20 and 30 mm downstream the injector nozzle and correspond to the PDA measurement stations. As visible in Fig. 8, the agreement is both qualitative and quantitative. In fact, the overall

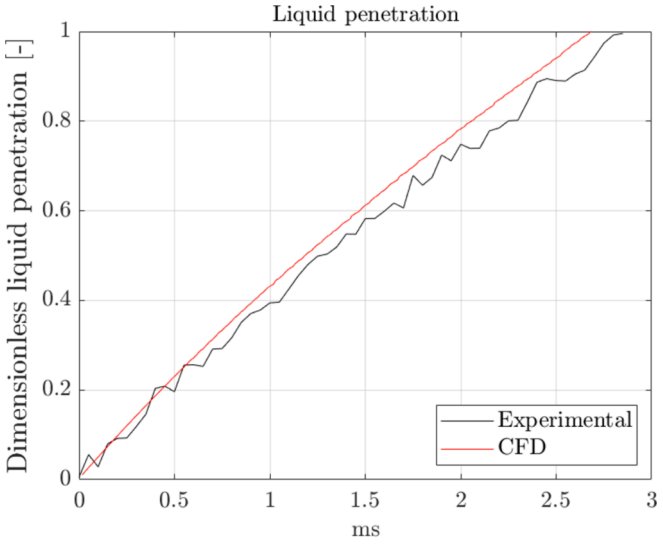

Fig. 6. Numerical-experimental comparison in terms of liquid spray penetration. Values are made dimensionless dividing both the set of data by the maximum experimental value.

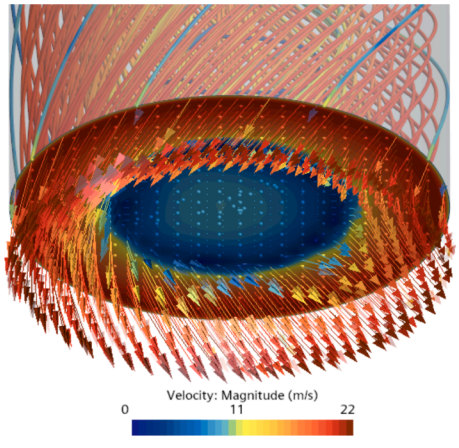

a)

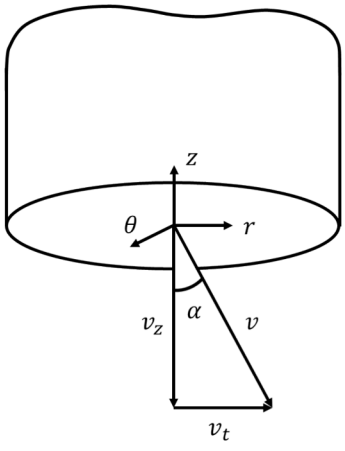

b)

Fig. 5. (a) shows streamlines inside the nozzle hole and velocity vectors at the outlet; (b) reports the cylindrical coordinate system and the components of the mean velocity at the nozzle outlet.

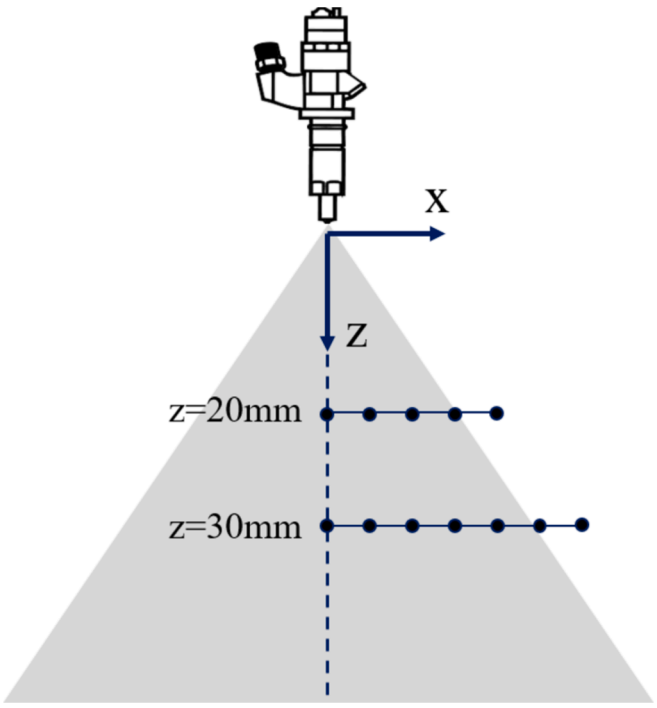

Fig. 7. Measurement stations.

trend of diameters and velocities as a function of the distance from the axis is matched. Moreover, numerical and experimental values are close at each monitor point. The discrepancies are minimal and mainly due to the model assumptions. Firstly, the methodology developed for the droplet initialization (as an alternative to primary breakup modelling) results to be effective but it is not devoid of approximations, such as the adoption of a RR distribution or even the calculation of d_0, effective droplet velocity and outer cone angle by the dedicated internal nozzle flow simulation. The secondary break-up modelling includes assumptions too. For example, droplets usually experience different break-up mechanisms. However, the adoption of the Reitz-Diwakar implies that only two mechanisms (namely bag and stripping) are considered. Moreover, the Reitz-Diwakar model is not strictly predictive, that is, based on the operating conditions, it requires calibration of the constants. In other words, the latter can represent a source of misalignment between simulations and experiments (so they can be further and more finely calibrated to improve the numerical results). However, it is important to point out the accuracy of the simulation outcomes. In fact, although there are errors of even 50 % considering the PDA comparisons, the gap is in most of the cases lower than the standard deviation of the experimental datum. Moreover, considering the droplet diameters, the graphs (that are dimensionless for confidentiality reasons) show comparisons on sizes that are in the order of few microns. Therefore, even if in relative terms the errors are not negligible, in absolute terms the discrepancies are minimal.

For confidentiality reasons, it is not possible to show spray imaging. However, thanks to both the estimated outer cone angle and the calibrated inner one, the spray morphology is well reproduced.

3.3. Stripping modeling

The droplet-wall interaction is governed by the Bai-ONERA model [15,30,31], characterized by the calibration constants reported in Table 2.

Among the different tasks, the model establishes the criteria for the formation of liquid film. If large amounts of film are formed, stripping may occur. In the present study, film formation as well as stripping are massive in the prefilmer. Since a proper modelling is crucial to reliably simulate the burner operation, an in-house approach to the stripping modelling is developed and described in the following.

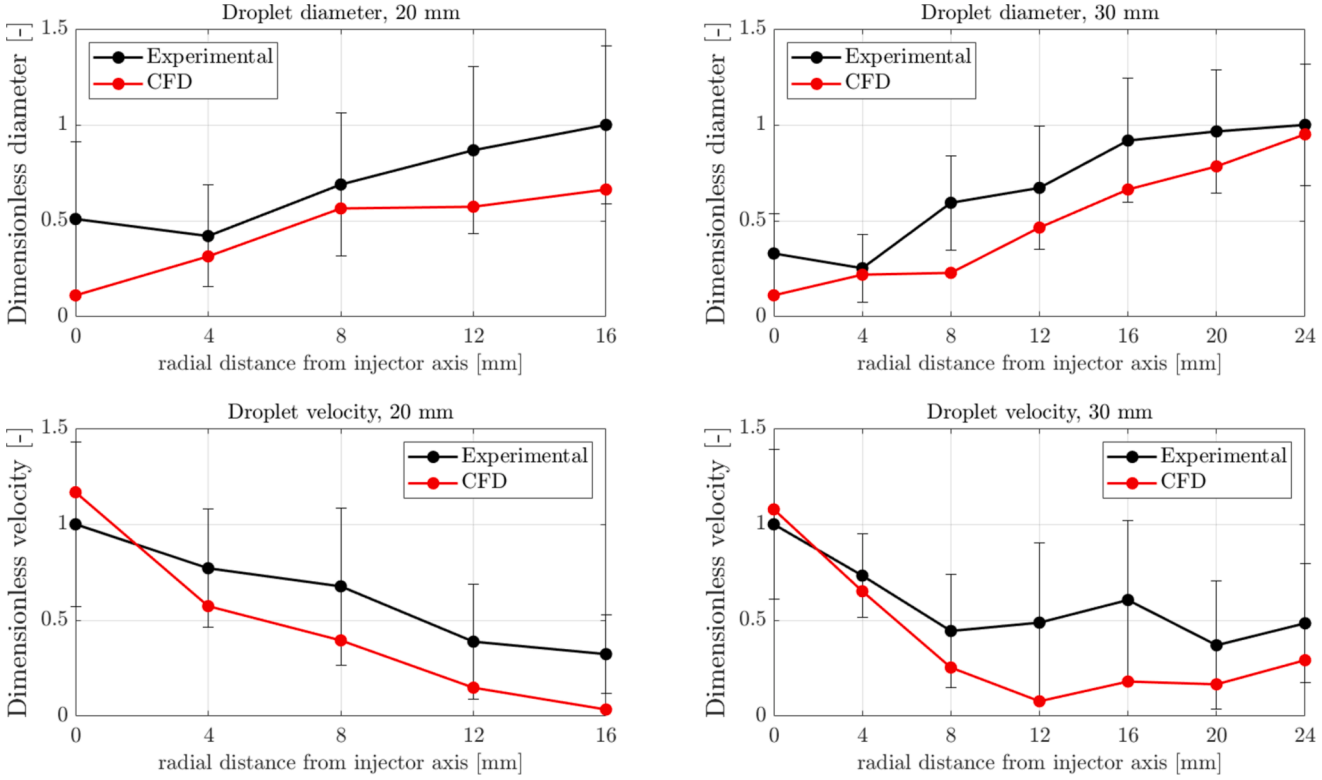

Fig. 8. Comparison between CFD and experiments in terms of droplet diameter and velocity; black bars represent the standard deviation of the experimental measurements. In each graph, both numerical and experimental data are made dimensionless dividing by the maximum experimental value.

Table 2
Bai-ONERA calibration constants. A_w is an empirical coefficient that can be modified to alter the threshold of the droplet incidence Weber number that separates spread or splash regimes in case of impingement on a wetted wall. c_f is the wall friction coefficient that scales the tangential velocity of the rebounded drops. n is an exponent that can be adopted to adjust the secondary-to-incident mass ratio r_{ds}, the latter expressing the mass fraction of the incident drop that is transferred to the rebounded child droplets after splash.

A_w	3000
c_f	0.6
n	1

The approach to stripping proposed in the present paper relies on Bertodano's findings. In [32], Bertodano defines, investigating the stripping in a pipe, a characteristic Weber number as in Eq. (5), where ρ is the gas phase density, σ the liquid surface tension, U_{mean} the mean flow velocity in the pipe and D the diameter of the pipe itself.

$$We_g = \frac{\rho U_{mean}^2 D}{\sigma} \tag{5}$$

Then, Bertodano defines E as in Eq. (6). It is the ratio between the mass flow rate of the stripped droplets and the film mass flow rate.

$$E = \frac{\dot{m}_{strip}}{\dot{m}_{film}} \tag{6}$$

In [32], thanks to the experiments, Bertodano obtains a correlation between We_g and E. As a proof of this, Fig. 9 reports Bertodano's experimental results. In the present work, in order to exploit such results, a fitting function is adopted, which approximates Bertodano's findings and whose definition is proposed in Eq. (7). The fitting function is visible in Fig. 9.

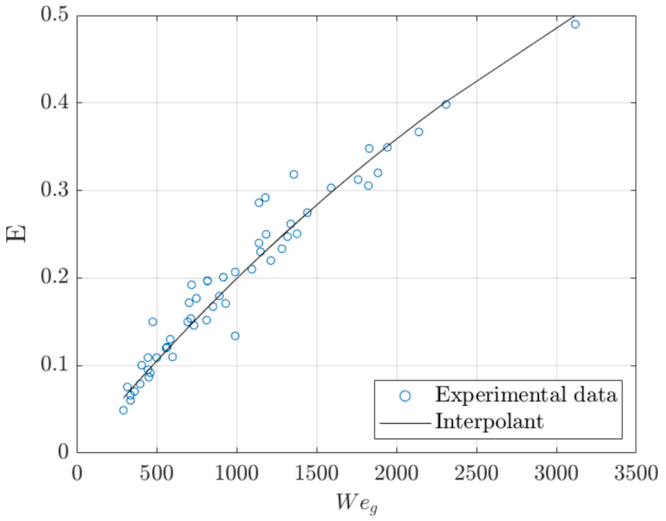

Fig. 9. E (Eq. (6)) is reported as a function of the Weber number (Eq. (5)). In particular, the blue circles represent the experimental data collected by Bertodano [32], while the black line corresponds to their fitting function adopted in the present paper (Eq. (7)). In detail, each circle represents a specific condition tested by Bertodano, who collects, for each single experiment, mass flow rates of stripped droplets and film and, then, calculates E according to Eq. (6).

$$E = 1 - \exp\left(-\frac{We_g}{4500}\right) \tag{7}$$

In the present 3D simulations, once We_g is calculated in the prefilmer (which is de facto a small pipe), the parameter E is estimated thanks to Eq. (7). However, still in the CFD framework, E can also be computed following Eq. (8) where, coherently with the definition proposed by Bertodano, the first fraction represents the mass flow rate of stripping film (i.e. stripping droplets), while the second fraction is the inverse of the liquid film mass flow rate.

$$E = \frac{N\ \pi\ SMD^3\ \rho_l}{6\ ts}\ \frac{1}{h\ w\ v_l} \tag{8}$$

N is the number of droplets stripped at each iteration and characterized by a Sauter mean diameter equal to SMD. ρ_l is the droplet density, while ts is the timestep. h and w are film thickness and width. For each computational cell, w corresponds to the width of the cell itself. v_l is the film velocity component parallel to both wall and prefilmer axis. In Eq. (8), SMD is computed by an in-house developed fit of experimental data that are obtained by Gepperth in [33], for different film spreading lengths in the streamwise direction and different air velocities. The fit proposed in the present paper is reported in Eq. (9) and it is obtained following the same procedure proposed by Gepperth in [34] based on Buckingham-π-theorem: it is a function of film spreading length in the streamwise direction, film thickness, film chemical properties and gas velocity.

$$SMD = 0.358\ L^{0.692}\ Re_x^{-0.17}\ We_x^{-0.36}\ \left(\frac{\rho_g}{\rho_l}\right)^{-0.013} \tag{9}$$

L is the film spreading length, $Re_x = \frac{\rho_g u_g \delta_x}{\mu_g}$ the Reynolds number and $We_x = \frac{\rho_g \delta_x {u_g}^2}{\sigma}$ the Weber number. σ is liquid surface tension. Reynolds and Weber numbers are computed by both characteristic length equal to the local boundary layer thickness δ_x and gas velocity u_g. ρ_l and ρ_g are densities of liquid film and gas.

Still in Eq. (8),v_l is modelled following Govan's [35] assumption for annular flows, i.e. it is considered equal to the 10 % of the pipe mean flow velocity U_{mean}.

Resuming, in Eq. (8) (considered as implemented in the CFD code), ρ_l, ts, h and w are provided by the solver. SMD and v_l are obtained by correlations and E is known thanks to Eq. (7). The only unknown of Eq. (8) is n. Therefore, in the CFD framework, such equation provides the number of droplets with diameter SMD that strip from each computational cell.

Noteworthily, stripped droplets can undergo secondary breakup, which is modelled in the same way as for the spray droplets (i.e. by Reitz model).

Before moving to the results, it is necessary to point out that a calibration constant multiplying the droplet diameter (SMD) is introduced and set equal to 0.7, to improve the match of the numerical results with the experiments. Firstly, the value of the constant is close to 1, so the calibration is minimal. Secondly, the need for a calibration is definitely understandable, as a consequence of the assumptions included in the stripping modelling. For example, all the adopted fits are obtained starting from experimental data of simple taste cases whose geometries differ from the burner one. Another strong assumption deals with v_l. However, such assumptions are crucial to obtain an effective model that can be easily implemented in the CFD code.

4. Results

4.1. Framework validation

In order to validate the 3D-CFD simulations with the test rig

outcomes, temperature and emissions measurements are compared. For the scope, a probe replicating the experimental thermocouple is inserted at the outlet of the virtual burner. In addition, emissions are measured in the CFD model in the exact position where they are sampled in the tests. The comparison between simulation and experiments is presented in Table 3. The proposed values represent time-averages computed during the steady-state operation of the burner. Both the combustion models provide an estimation of the gas temperature close to the experimental counterpart (the error is lower than 4 %). In addition, NO concentration (which is tightly related to the maximum temperature inside the burner) is properly matched by the simulations. Therefore, it is possible to state that the thermal field inside the burner is well captured by the CFD. Since temperature is, in turn, strongly dependent on the combustion efficiency, it is reasonable to confirm the effectiveness of the two tested models to simulate combustion inside the device. A further confirmation comes from the comparison in terms of CO concentration, which represents a clear indicator of combustion efficiency. Both ECFM-3Z and DC are again able to properly predict the order of magnitude of the CO concentration. It is interesting to point out that results in terms of temperature and CO concentration are coherent. In fact, ECFM-3Z provides an exhaust gas temperature which is slightly higher than the experimental counterpart and, coherently, it underpredicts the CO concentration. Conversely, DC slightly underestimates the exhaust gas temperature and, as a consequence, it provides a CO concentration higher than expected. Finally, if temperature and emissions are reasonably captured by CFD, it means that also the modelling of the liquid film is effective. Specifically, both accumulation and stripping are properly predicted.

There are two other key points before moving on with the discussion. Firstly, the proposed results are obtained without ad-hoc calibration of the combustion models, i.e. default settings are kept. Secondly, although both the tested combustion models prove to be effective for combustion simulations inside the burner, the result discussion presented in the following deals solely with ECFM-3Z outcomes. This is done for the sake of simplicity. In fact, as it will be shown in the next paragraphs, burner operation is characterized by the presence of both premixed and diffusive combustion. In each computational cell, ECFM-3Z automatically separates the heat release of each mode, and it allows a more straightforward analysis of the results. On the contrary, for DC, a more complex approach should be adopted, for example introducing Takeno Index [36].

4.2. Result analysis: Flow field, spray, liquid film and mixture formation

The analysis starts with the velocity field in the combustion chamber. Fig. 10 shows the streamlines inside prefilmer and combustion chamber. Specifically, a swirling motion is visible, coaxial with the combustion chamber and directed towards the outlet. It is created by the swirler and is conserved in the main chamber thanks to the adhesion to the prefilmer wall, as demonstrated by the red strips at the prefilmer outlet, visible in Fig. 11, which shows the streamlines on a section parallel to the burner axis. The low pressure associated to the vortex core is responsible for the secondary motion that can be noticed in Fig. 11. It is responsible for a backflow towards the prefilmer. Such a secondary motion can be usefully exploited to retain the injected fuel inside the chamber, thus promoting mixing and combustion. It is important to point out that Figs. 10 and 11 show the steady-state cold flow, i.e. neither injection nor combustion are included. Moreover, although combustion is simulated in STAR-CD, such cold flow images are provided by STAR-CCM+. However, the images are rigorously obtained by grid and results imported from STAR-CD. The reason for this step is that STAR-CD does not offer streamlines among the post-processing tools. In addition, in the same images and in the following ones, the geometry of the swirler in never shown for confidentiality reasons.

Table 3
Comparison between 3D-CFD and experiments in terms of exhaust gas temperature and emissions.

	T [°C]	NO [ppm]	CO [ppm]
EXP	**1142**	**30**	**665**
ECFM-3Z	1186	22	290
Detailed Chemistry	1107	24	1257

Moving to the injection process, the resulting spray is visible in Fig. 12(a). In the same figure, the stripped droplets are reported as well, with a different color, to distinguish them from the injected ones. Fig. 12 (b) shows the liquid film on the walls of the domain. Firstly, it is due to the spray droplets impinging onto the wall of the prefilmer. Secondly, only the latter is massively involved in the formation. For all the other boundaries, the amount of film is negligible. Therefore, Fig. 12(a) and (b) represent the numerical evidences of the prefilmer working principle discussed in Fig. 3, i.e. the spray impinges the prefilmer wall and, from the latter, droplets strip entrained by the rapid air flow. The mixture resulting from injection, film formation, stripping and evaporation is visible in Fig. 12(c). Interestingly, the evolution of φ is characterized by a delay compared to the injection. In other words, injection starts at ~0 ms while the increase of φ is visible only from 2 ms and on. Similarly, when the injection terminates (at ~6 ms), φ reduces with a delay (i.e. only after 8 ms). The reason for such delays is due to the different phenomena interposing between spray and mixture formation. Before moving to the analysis of combustion efficiency, it is useful to point out that the images reported in Fig. 12 refer to the steady-state operation of the burner and they start with an injection event and terminate at the start of the subsequent injection event. Since the injection frequency is 100 Hz, the period covered by the images is 10 ms.

4.3. Result analysis: Combustion efficiency

The computed heat release rate in the whole domain is reported in Fig. 13. A time window of 0.5 s is considered, which is widely representative of the burner at steady state condition, as it accounts for several injections and sparks. On average, the heat release rate is equal to ≈17 kW. Although the whole domain (burner with sampling pipe) is considered for the computation, more than 95 % of the thermal power is released inside the burner and in a small portion of the sampling pipe (10 cm).

Considering a gasoline lower heating value of 42900 kJ/kg (adopted in the simulation), the resulting internal efficiency of the burner can be computed as in Eq. (10), where the heat release rate *HRR* is considered.

$$\eta_{internal} = \frac{HRR}{\dot{m}_{inj}\ LHV} = 76.8\% \tag{10}$$

$\dot{m}_{inj}$ and *LHV* are mass flow rate and lower heating value of the injected gasoline, respectively. Considering, instead of the injected mass flow rate, the difference between total injected mass and total accumulated liquid film mass, it is possible to compute the amount of gasoline that can effectively take part to the reactions and, hence, to calculate the combustion efficiency. In this second case the heat released (computed by time integration of the rate) is used for the efficiency calculation, as in Eq. (11).

$$\eta_{comb} = \frac{HR}{\left(m_{inj} - m_{film}\right)\ LHV} = 98.2\% \tag{11}$$

HR, m_{inj} and m_{film} are heat released by the burner, injected fuel mass and accumulated liquid film mass, respectively. For the present analysis, these quantities are evaluated on the time window mentioned above, representative of the steady-state behaviour of the burner. As visible in Fig. 14, in the investigated period, 21.8 % of the injected mass transforms into liquid film, thus only 78.2 % can be exploited for combustion.

Such fraction of gasoline (corresponding to $m_{inj} - m_{film}$) can be meant as prefilmer efficiency, that is the capability of the prefilmer to convert

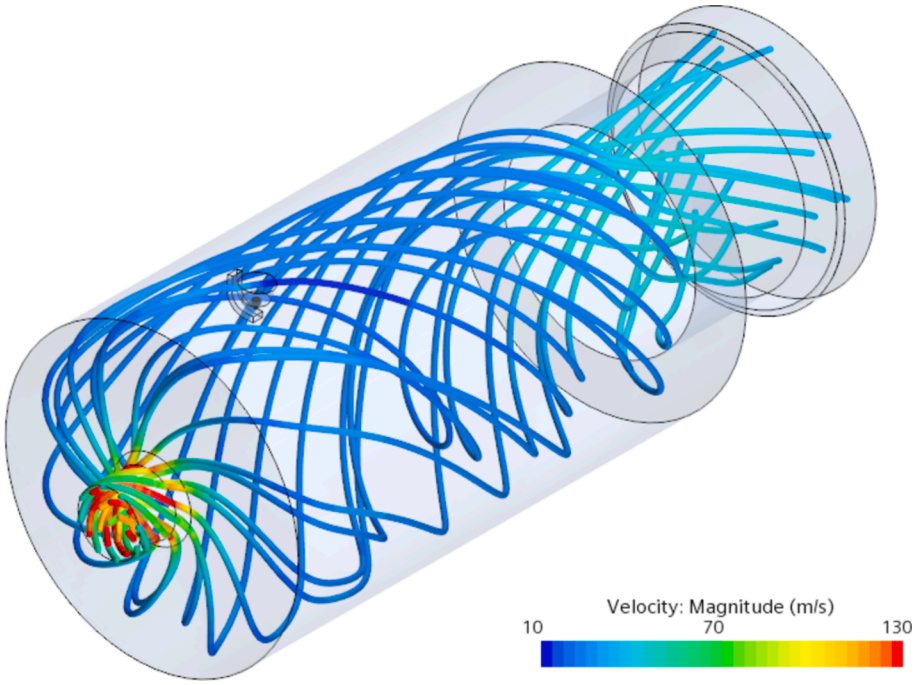

Fig. 10. Streamlines inside prefilmer and combustion chamber.

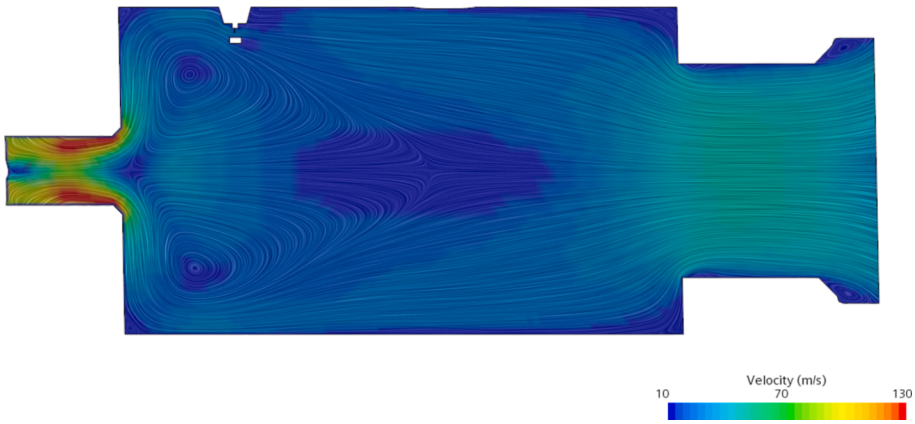

Fig. 11. Velocity field magnitude and streamlines on an axial section.

liquid film into droplets, as resumed by Eq. (12).

$$\eta_{prefilmer} = \frac{m_{inj} - m_{film}}{m_{inj}} = 78.2\% \tag{12}$$

The internal efficiency relies on the heat release rate which includes both the useful heat (i.e. the one available at the exhaust) and the heat loss at the walls. However, in order to calculate the global efficiency of the system, only the useful heat at the exhaust should be considered. For this reason, the adiabatic efficiency has to be included. The heat loss rate at the walls under steady state operation is proposed in Fig. 15 for the same time window previously considered. The average value is roughly 4.6 kW.

Then, the adiabatic efficiency is computed as in Eq. (13).

$$\eta_{ad} = \frac{HRR - HT}{HRR} = 73.1\% \tag{13}$$

HT is the average wall heat transfer under steady-state operation.

Since the actual useful effect of the burner is the thermal power available at the exhaust gases, the global efficiency can be computed as in Eq. (14).

$$\eta_{tot} = \frac{HRR - HT}{\dot{m}_{inj}\ LHV} = 56.1\% \tag{14}$$

Finally, combining Eqs. (11)-(14), it is straightforward to notice that the total efficiency can be expressed as in Eq. (15), i.e. as the product of all the efficiencies previously calculated.

$$\eta_{tot} = \eta_{prefilmer}\ \eta_{comb}\ \eta_{ad} \tag{15}$$

Thanks to the analysis of the efficiencies, it is possible to identify the limiting factors of the proposed prototype. In particular, it is necessary to improve the strategy of break-up and evaporation via a more effective prefilmer, able to avoid massive accumulation of film on its surface. Moreover, the adiabaticity of the burner has to be promoted by reducing the heat losses at the walls.

4.4. Result analysis: Combustion mode

The heat release rate is examined in the present paragraph, in order

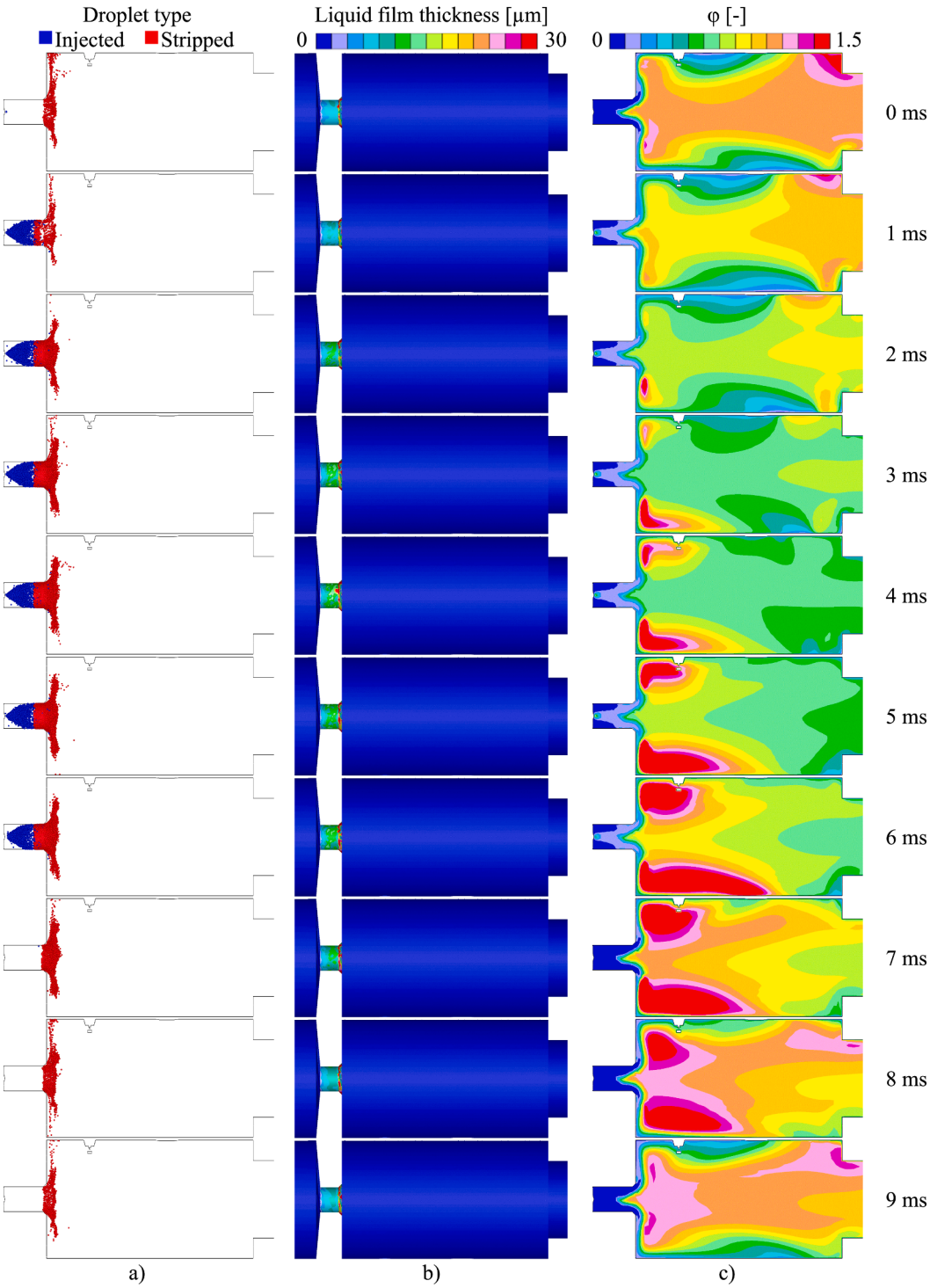

Fig. 12. (a) injection spray (in blue) and stripped droplets (in red); (b) liquid film on the walls of the domain; (c) equivalence ratio.

to investigate the combustion mode inside the burner. Thanks to the capabilities of ECFM-3Z, the total HRR can be split into diffusive and premixed (as well as for auto-ignition but it is not of interest in the present work) and the two are shown in Fig. 16(a) and (b), respectively. As shown in Fig. 12(a), droplets are carried by the fluid towards the periphery of the combustion chamber. Part of the fuel already burns at the corners, as visible in Fig. 16(a), thanks to the available air. Meanwhile, the remaining portion mixes with the air and gives raise to premixed combustion both in the primary swirling flow directed towards the exhaust pipe and inside the secondary motion (the back flow previously described).

From a quantitative standpoint, Fig. 17 reports the amounts of heat release rate for both premixed and diffusive combustion for the previously considered time window, i.e. during the steady-state operation. It is possible to notice the relevance of the diffusive combustion mode. In detail, 34.8 % of the total heat is released by diffusive combustion, while the remaining percentage (64.2 %) comes from premixed mode. This analysis is of primary importance in order to minimize the emissions of the burner (which should be close to 0). In fact, the presence of diffusive combustion can locally lead to soot production as well as temperature

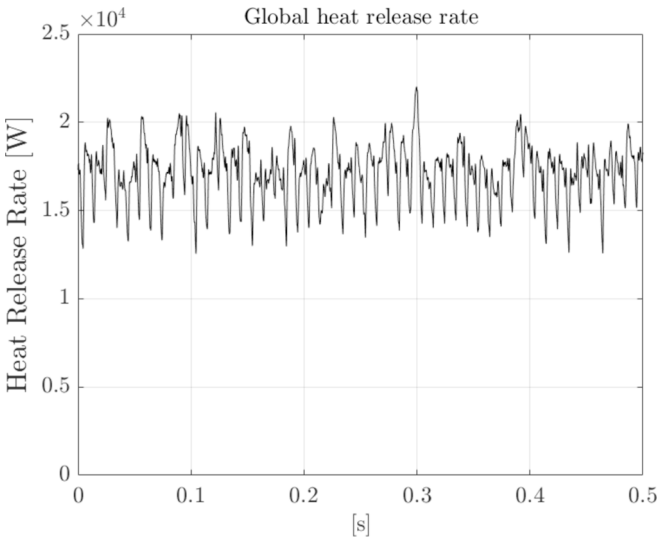

Fig. 13. Heat release rate in the whole domain.

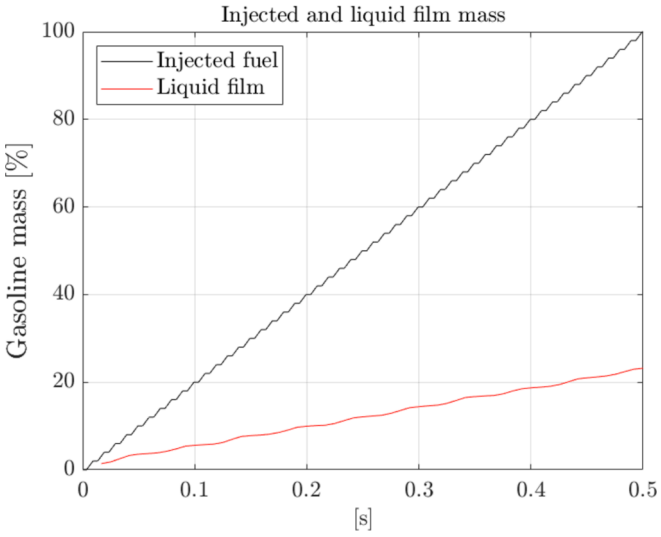

Fig. 14. Cumulative injected and liquid film masses.

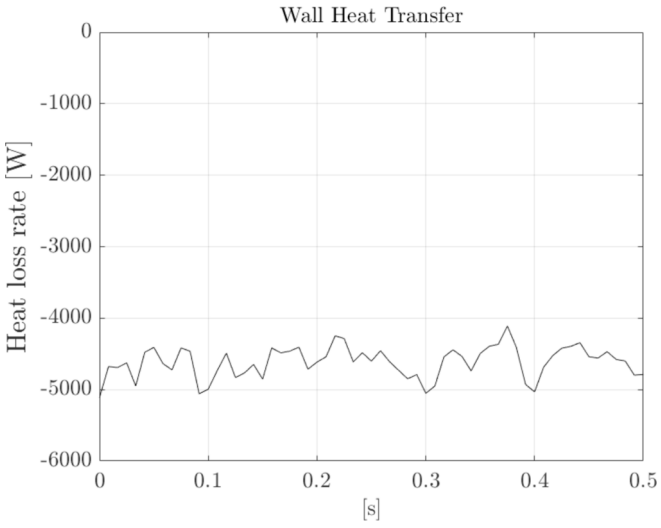

Fig. 15. Heat transfer at the burner walls.

peaks, which in turn promote NO_x formation, like in Diesel engines. The fact that almost 1/3 of the heat is released by diffusive mode suggests the need of intervention in terms of design or operating conditions of the burner, in order to improve evaporation and mixing and, thus, promoting premixed combustion. In this regard, Fig. 18 shows NO concentration inside the chamber and, as visible, it is higher close to the regions where the diffusive HRR is strong.

It is interesting to point out that, similarly to the experiments, once the burner reaches a steady state condition, the numerical ignition is turned off. This occurs at 0.2 s where the heat release rate is unaffected, as visible in Figs. 13 and 17, as a further demonstration that simulations well agree with the experimental evidences.

4.5. Result analysis: Combustion regime

Before moving to the conclusions, an analysis of the combustion regime inside the burner is carried out, and the applicability of the adopted combustion models is discussed.

The regime diagrams for both premixed and diffusive combustion are proposed in the following, in order to investigate the behaviour of the burner under steady-state operation. In a generic cell of the CFD model, the combustion mode is identified by the occurrence of premixed or diffusive heat release rate. As a consequence of the ECFM-3Z capabilities, premixed and diffusive combustion modes can be present at the same time in each cell of the domain. Therefore, each cell can be simultaneously used to calculate the average combustion regime of the burner for both premixed and diffusive combustion. In this regard, the average regime for each mode is calculated by means of all the cells of the burner presenting the considered combustion mode. In each of those cells, the regime is calculated and, then, the average regime is computed using the heat release rate as weight. For example, considering premixed combustion, all the cells where heat release rate by premixed combustion occurs are considered. In each cell, the combustion regime is calculated. For the entire burner, the average regime is computed using the heat release rate by premixed combustion as weight. The higher the heat release rate is in a cell, the more representative that cell is of the burner behaviour. For diffusive combustion, the calculation of the average regime takes place in a similar way. Simply, the cells showing the presence of diffusive combustion are accounted for.

Focusing on premixed combustion, in the cells characterized by the presence of premixed heat release rate, the ratios $\frac{u'}{S_l}$ and $\frac{l_t}{\delta}$ are computed, where u' and S_l are root mean square of turbulent velocity fluctuations and laminar flame speed, while l_t and δ are integral length scale and laminar flame thickness. Then, the average values of the ratios on the cells showing premixed combustion are computed using the premixed heat release rate as weight, so that it is possible to identify a point in the combustion regime diagram. This process is repeated at each time-step in order to show, inside the diagram of Fig. 19, the burner behaviour over the time. It is interesting to point out that, during the steady-state operation, the device is characterized by a cyclic behaviour, with periodicity determined by the injection process. Therefore, also the combustion process is periodic. For this reason, the regime in Fig. 19 is represented by a closed loop which repeats over time. For clarity of the representation, only one cycle is shown in Fig. 19.

In this last, the laminar combustion regime is delimited by the black dashed line ($Re_t = 1$), while solid black and solid grey lines correspond to $Ka = 1$ and $Da = 1$. Such quantities are computed as $Da = \frac{Sl}{u'} \frac{l_t}{\delta}$ and $Ka = \frac{u'}{Sl} \frac{\delta}{\eta_t}$, where η_t is the Kolmogorov turbulence scale and $Re_t = \frac{u'}{Sl} \frac{l_t}{\delta} = Ka^2 Da^2$. $Da < 1$ and $Ka < 1$ regions correspond to "well-stirred reactor" and "flamelet" combustion regimes, respectively. The area included between $Da = 1$ and $Ka = 1$ corresponds to the "thickened flame" regime, where a flame structure is still present but with an increased thickness. This is due to the ability of the small scales of turbulence to penetrate the flame front, enhancing the mixing. As visible in

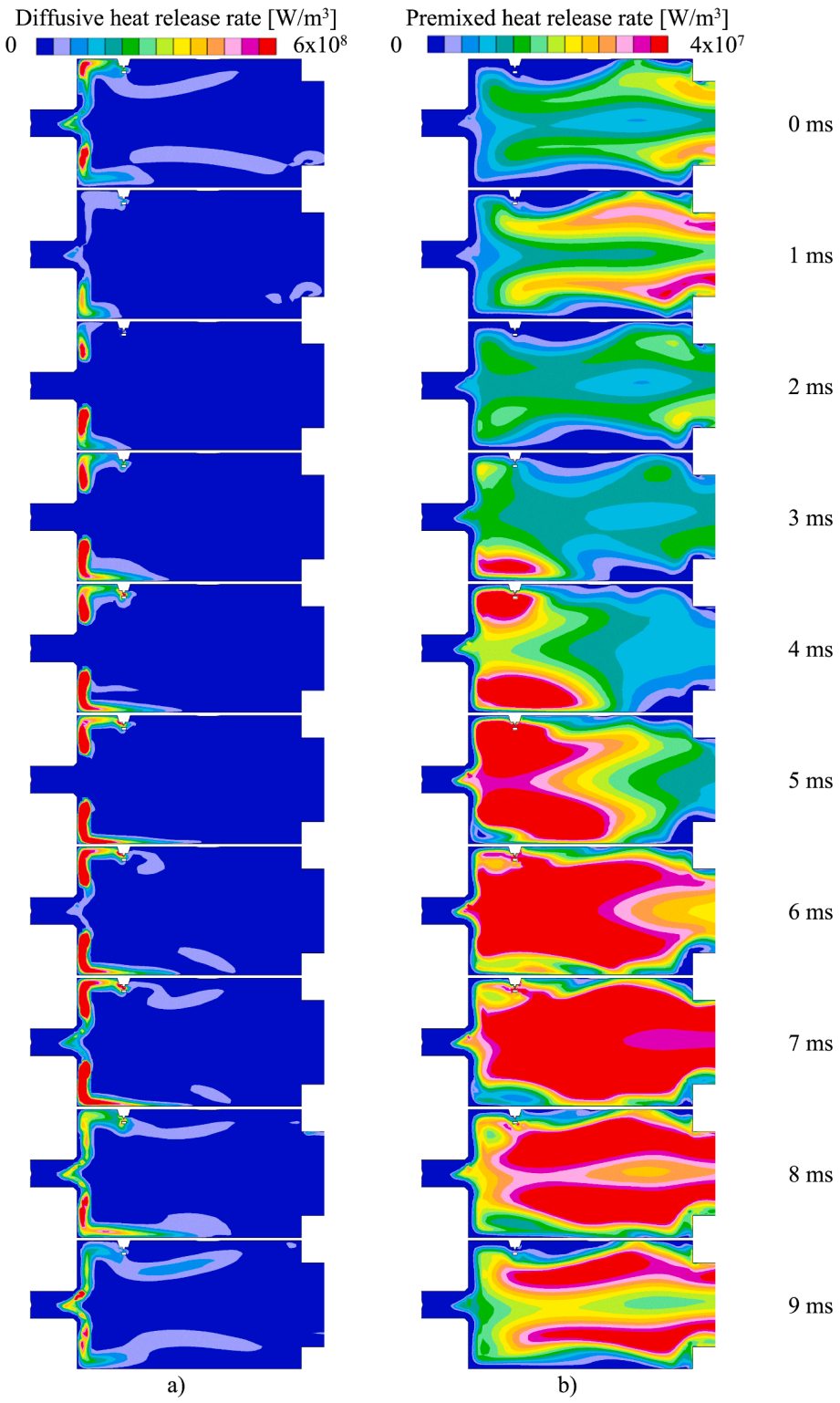

Fig. 16. (a) diffusive heat release rate; (b) premixed heat release rate. For completeness, it is useful to point out that these images refer to the same injection event reported in Fig. 12.

figure, the loop representing the burner behaviour lays in the region representing the thickened flame regime.

Moving to the diffusive combustion, the description of the regime inside the burner relies on a different diagram. In this case, the bi-logarithmic axes report Damkohler number Da and turbulent Reynolds number Re_t. In the currently investigated combustion mode, Da is calculated as $Da = \frac{l_t/u'}{\tau_c}$, where τ_c is a chemical time scale equal to $\tau_c = A\, e^{\frac{T_a}{\widetilde{T}_b}}$. A and T_a are a constant and the activation temperature equal to $2 \bullet 10^{-6}$ and 6000 K, respectively. $\widetilde{T}_b$ is the Favre-average burnt temperature in the cell. This expression for τ_c is inherited from [37], where A and T_a are validated on engine cases. As for Re_t, it is $Re_t = \frac{u' l_t}{\nu}$, where ν is the kinematic viscosity. The average values of Da and Re_t on the cells showing diffusive combustion are computed using the diffusive heat

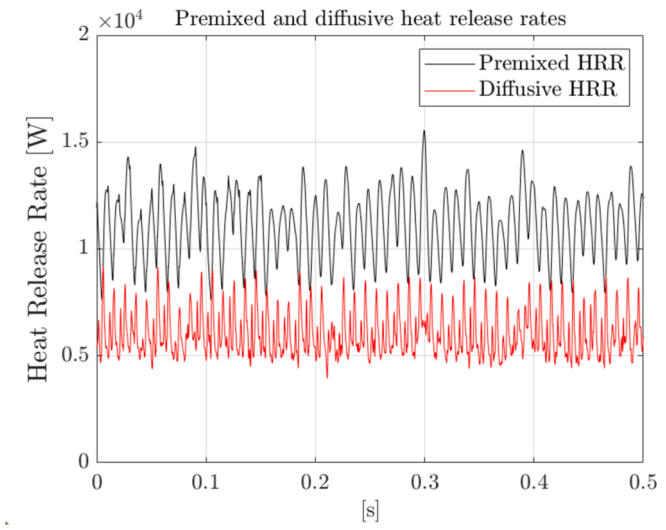

Fig. 17. DIffusive and premixed heat release rates.

release rate as weight, so that it is again possible to identify a point in the combustion regime diagram. Similarly to Fig. 19, this process is repeated at each time-step in order to obtain the burner behaviour over the time, as visible in Fig. 20. Even in this case, the device is characterized by cyclic behaviour during combustion at steady-state condition, with periodicity still determined by the injection. For this reason, the regime in Fig. 20 is represented once again by a closed loop which repeats over the time. Only one cycle is shown in Fig. 20, for clarity. Focusing on the diagram, laminar and turbulent combustion regimes are separated by the $Re_t = 1$ dashed line, while solid black and grey lines are the ones at $Da_{fl} = Da_{lfa}$ and $Da_{fl} = Da_{ext}$, respectively. Da_{fl} is computed as $\frac{Da}{2\sqrt{Re_t}}$, while Da_{lfa} and Da_{ext} are equal to 0.4 Da_{se} and 2 Da_{se}, respectively. Da_{se} is the Damkohler number at which a steady laminar stagnation point flame extinguishes. Da_{se} is computed by a DNS simulation in [38] and it is found equal to $5.098 \bullet 10^{-3}$. Da_{ext} represents the limit Damkohler number under which strain-induced turbulence leads to flame extinction, while Da_{lfa} is the limit over which combustion is purely flamelet. Unsteady effects occur in the middle range. The definitions of Da_{fl}, Da_{lfa}, Da_{ext} and Da_{se} proposed above and the construction of the diffusive combustion diagram are inherited from [39]. As visible in Fig. 20, the different (average) combustion regimes that form the cycle representing the burner behaviour pertain to the flamelet region, where combustion is characterized by a very thin and laminar flame, wrinkled by turbulence.

Since ECFM-3Z is a flamelet combustion model, its adoption is fully justified only for the diffusive combustion modelling inside the burner. On the contrary, its applicability is formally incorrect for the premixed part, which is characterized by the thickened flame regime. Nonetheless, the validation proposed above reveals that this model is capable to fairly predict premixed combustion even in the thickened flame regime. This is coherent with the available literature on reciprocating ICEs. In fact, multiple works [40–42] show that in-cylinder simulations are characterized by the presence of multiple coexisting combustion regimes and flamelet models are still able to provide promising results. As suggested by d'Adamo et al. [40], this is possible thanks to the calibration of the model coefficients. These are carefully chosen by the developers to allow a proper operation of the models in actual cases which are characterized, as stated above, by a wide range of simultaneously present regimes.

Similarly, DC should not be adopted to simulate premixed combustion at thickened flame regime or diffusive combustion at flamelet conditions, unless turbulence is fully resolved (and this is not the case as a RANS approach is adopted). However, also for DC, the previously presented validation confirms the capabilities of such a model to simulate combustion even at flamelet regime. This is not a novelty in literature. In fact, multiple publications [43–51] show a satisfying agreement between CFD and experiments, when DC is adopted to simulate the wide range of regimes typical of reciprocating ICEs [40–42]. It is important to point out that DC is effective also with thickened flame and flamelet combustion regimes not by chance. In fact, as suggested in [52], the adoption of scaling factors to tune reaction rates and diffusion (as those present in the STAR-CD default settings) is common to compensate the lack of turbulence-flame interaction modelling. Similarly to ECFM-3Z, such a scaling is purposely introduced in order to increase the predictive capabilities of DC over a wide range of regimes, which are often coexisting in actual industrial problems.

5. Conclusions

In this work, a numerical framework is presented for 3D-CFD simulations of gasoline fuelled burners to be adopted in catalyst preheating operations. The proposed framework relies on purposely developed approaches for modelling of spray and liquid film stripping. As for the spray, it is generated by a hollow cone swirling injector and it is modelled via a lagrangian approach. Droplet initialization in terms of

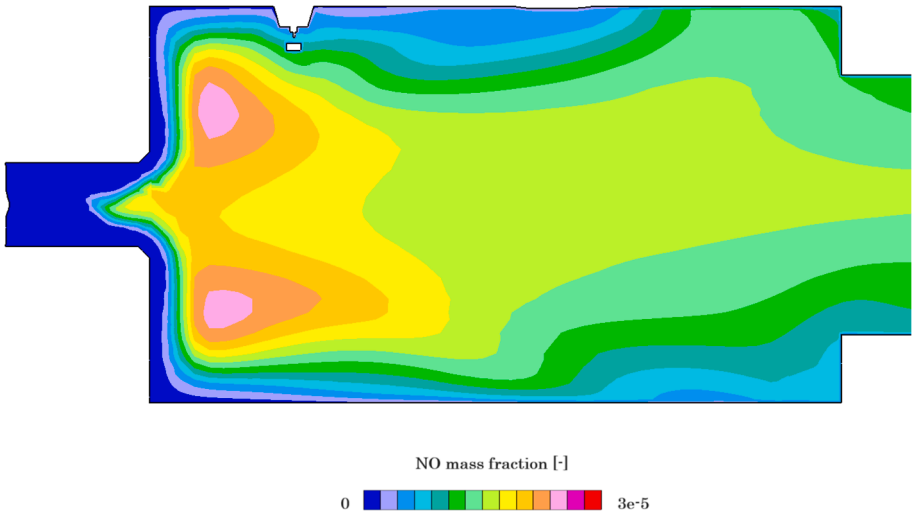

Fig. 18. NO mass fraction on a section parallel to the combustion chamber axis. This image refers to the same injection/combustion event described in Figs. 12 and 16; in particular, this picture is taken at 8 ms.

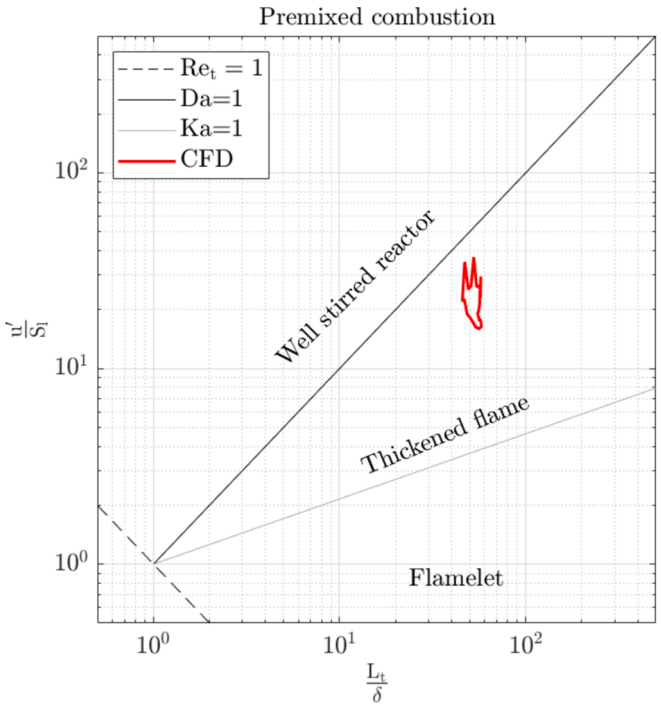

Fig. 19. Regime diagram for premixed combustion.

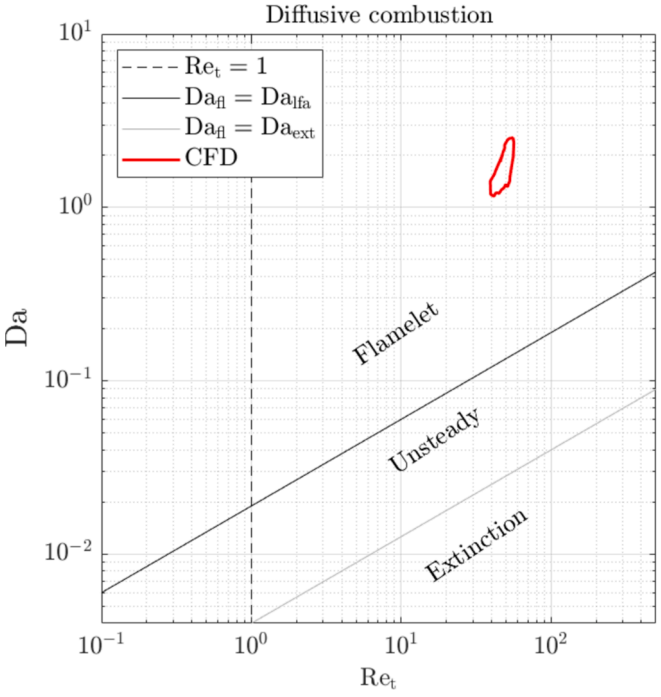

Fig. 20. Regime diagram for diffusive combustion.

diameter and velocity is one of the most critical aspects and it is obtained by a dedicated internal nozzle simulation. The resulting lagrangian spray is then validated against experimental data. As for the stripping, the proposed approach is able to provide velocity, diameter and number of droplets involved in the phenomenon as well as the overall mass flow rate of fuel living the wall. Two different combustion models are tested, namely ECFM-3Z and DC, both widely adopted in literature for in-cylinder simulations. In fact, the main goal of the present work is the proposal of a numerical framework based on best practice for in-cylinder analyses of SI ICEs, in order to prove that a single setup can be exploited to analyse multiple devices with saving of cost and time. The proposed framework is successfully validated against experimental data of gas temperature and emissions on an in-house designed prototype of burner. Both the combustion models are able to properly match the experimental outlet temperature, with an error lower than 4 %. As for the emissions, ECFM-3Z and DC are able to predict, at least as order of magnitude, the ppm concentrations of NO and CO at the exhaust. Overall, a good agreement is obtained between simulations and experiments with both the models. Once validated, the utility of the proposed numerical framework is demonstrated. In fact, it is employed to deeply investigate the burner in terms of flow field, mixture formation, efficiency and combustion mode. The most critical aspects are found to be liquid film formation and wall heat losses, which strongly penalize the global efficiency. In particular, prefilmer and adiabatic efficiencies result equal to 78.2 % and 73.1 %, which lead (along with a combustion efficiency of 98.2 %) to an overall efficiency of the burner of 56.1 %. Therefore, design improvements of the burner have to pursue a more effective droplet break-up (maybe by improved geometry of the prefilmer or even eliminating the prefilmer itself) and an optimized swirl motion (able to improve mixing without penalizing ignition). In addition, insulation is mandatory to reduce the losses at the walls. The main critical aspect of the presented framework is that the applicability of the adopted combustion models is restricted to specific conditions (for example ECFM-3Z should be adopted only for flamelet combustion). However, the proposed results show that, thanks to ad-hoc calibration, the effectiveness of the models can be proficiently extended to other regimes. It is finally useful to point out that the developed numerical framework can be adopted to simulate traditional and e-/bio-gasoline fuels.

Declaration of competing interest

The authors declare that they have no known competing financial interests or personal relationships that could have appeared to influence the work reported in this paper.

ACKNOWLEDGMENTS

The authors gratefully acknowledge the University of Modena and Reggio Emilia for supporting the activity by the “Fondo di Ateneo per la Ricerca 2024 per il finanziamento di piani di sviluppo dipartimentale nell’ambito della ricerca” (FARD 2024) and the “Fondi europei della Regione Emilia-Romagna”, within programs POR FESR e POR FSE 2014-2020 in the framework of the “Accordo Regionale di insediamento e sviluppo delle imprese – progetto BURNER”.

Data availability

The authors do not have permission to share data.

References

[1] Regulation (EU) 2023/851 of the European parliament and of the council, Official Journal of the European Union, OJ L 110.
[2] J. Gao, G. Tian, A. Sorniotti, A.E. Karci, R. di Palo, Review of thermal management of catalytic converters to decrease engine emissions during cold start and warm up, Appl. Therm. Eng. 147 (2019) 177–187, https://doi.org/10.1016/j.applthermaleng.2018.10.037.
[3] B. Bargman, S. Jang, J. Kramer, I. Soliman, A.A. Sahul, Effects of electrically preheating catalysts on reducing high-power cold-start emissions, in: SAE Technical Papers, SAE International, 2021, https://doi.org/10.4271/2021-01-0572.
[4] F. Mianzarasvand, A. Shirneshan, M. Afrand, Effect of electrically heated catalytic converter on emission characteristic of a motorcycle engine in cold-start conditions: CFD simulation and kinetic study, Appl. Therm. Eng. 127 (2017) 453–464, https://doi.org/10.1016/j.applthermaleng.2017.07.180.
[5] S. Canè, L. Brunelli, S. Gallian, A. Perazzo, A. Brusa, N. Cavina, Performance assessment of a predictive pre-heating strategy for a hybrid electric vehicle

equipped with an electrically heated catalyst, Appl. Therm. Eng. 219 (2023), https://doi.org/10.1016/j.applthermaleng.2022.119341.
[6] J. Hofstetter, P. Boucharel, F. Atzler, G. Wachtmeister, Fuel consumption and emission reduction for hybrid electric vehicles with electrically heated catalyst, in: SAE Technical Papers, SAE International, 2020, https://doi.org/10.4271/2020-37-0017.
[7] J. Gao, G. Tian, A. Sorniotti, On the emission reduction through the application of an electrically heated catalyst to a diesel vehicle, Energy Sci. Eng. 7 (6) (2019) 2383–2397, https://doi.org/10.1002/ese3.416.
[8] A. García, J. Monsalve-Serrano, R. Lago Sari, S. Martinez-Boggio, Energy assessment of an electrically heated catalyst in a hybrid RCCI truck, Energy 238 (2022) Jan, https://doi.org/10.1016/j.energy.2021.121681.
[9] J.S. Hepburn, A.A. Adamczyk, R.A. Pawlowicz, Gasoline Burner for Rapid Catalyst Light-off, 1994. https://doi.org/10.4271/942072.
[10] A.S.zu Schweinsberg, M. Klenk, A. Degen, Engine-Independent Exhaust Gas Aftertreatment Using a Burner Heated Catalyst, 2006. https://doi.org/10.4271/2006-01-3401.
[11] V. Rossi, L. Brocchi, M. Medda, S. Paltrinieri, F. Rulli, R. Tonelli, Design and Assessment of an Exhaust After-Treatment System Equipped with a Fuel, 2023. https://doi.org/10.4271/2023-01-0355.
[12] M. Battistoni et al., Burner Development for Light-Off Speed-Up of Aftertreatment Systems in Gasoline SI engines, 2022. https://doi.org/10.4271/2022-37-0033.
[13] A. Della Torre et al., Numerical Assessment of an After-Treatment System Equipped with a Burner to Speed-Up the Light-Off during Engine Cold Start, 2021. https://doi.org/10.4271/2021-24-0089.
[14] V. Yakhot, S.A. Orszag, Renormalization group analysis of turbulence. I. Basic theory, J Sci Comput 1 (1) (1986) 3–51, https://doi.org/10.1007/BF01061452.
[15] STAR-CD Methodology Guide.
[16] L. Teodosio, F. Berni, Optimization via genetic algorithm of a variable-valve-actuation spark-ignition engine based on the integration between 1D/3D simulation codes and optimizer, Int. J. Eng. Res. (2022), https://doi.org/10.1177/14680874221099874.
[17] F. Berni, et al., A zonal secondary break-up model for 3D-CFD simulations of GDI sprays, Fuel 309 (2022), https://doi.org/10.1016/j.fuel.2021.122064.
[18] C. Iacovano, et al., A Preliminary 1D-3D Analysis of the Darmstadt Research Engine under Motored Condition, in: E3S Web of Conferences, Vol. 197, EDP Sciences, 2020, pp. 1–12, https://doi.org/10.1051/e3sconf/202019706006.
[19] S. Sfriso, et al., Proposal and validation of a numerical framework for 3D-CFD in-cylinder simulations of hydrogen spark-ignition internal combustion engines, Int. J. Hydrogen Energy 53 (2024) 114–130, https://doi.org/10.1016/j.ijhydene.2023.12.027.
[20] S. Sfriso, F. Berni, S. Fontanesi, A. D'Adamo, M. Antonelli, S. Frigo, A 3D-CFD Numerical Approach for Combustion Simulations of Spark Ignition Engines Fuelled with Hydrogen: A Preliminary Analysis, 2023. https://doi.org/10.4271/2023-01-0207.
[21] F. Berni, G. Cicalese, M. Borghi, S. Fontanesi, Towards grid-independent 3D-CFD wall-function-based heat transfer models for complex industrial flows with focus on in-cylinder simulations, Appl. Therm. Eng. 190 (2021), https://doi.org/10.1016/j.applthermaleng.2021.116838.
[22] F. Berni, S. Fontanesi, A 3D-CFD methodology to investigate boundary layers and assess the applicability of wall functions in actual industrial problems: A focus on in-cylinder simulations, Appl. Therm. Eng. 174 (2020), https://doi.org/10.1016/j.applthermaleng.2020.115320.
[23] F. Berni, G. Cicalese, S. Sparacino, G. Cantore, On the existence of universal wall functions in in-cylinder simulations using a low-Reynolds RANS turbulence model, in: AIP conference proceedings, Vol. 2191, No. 1, AIP Publishing, 2019, https://doi.org/10.1063/1.5138752.
[24] M. Del Pecchia, V. Pessina, F. Berni, A. d'Adamo, S. Fontanesi, Gasoline-ethanol blend formulation to mimic laminar flame speed and auto-ignition quality in automotive engines, Fuel 264 (2020) 116741, https://doi.org/10.1016/j.fuel.2019.116741.
[25] A. D'Adamo, M. Del Pecchia, S. Breda, F. Berni, S. Fontanesi, J. Prager, Chemistry-Based Laminar Flame Speed Correlations for a Wide Range of Engine Conditions for Iso-Octane, n-Heptane, Toluene and Gasoline Surrogate Fuels, 2017. https://doi.org/10.4271/2017-01-2190.
[26] F. Berni, et al., Modeling of gaseous emissions and soot in 3D-CFD in-cylinder simulations of spark-ignition engines: A methodology to correlate numerical results and experimental data, Int. J. Engine Res. 24 (5) (2023) 2149–2174, https://doi.org/10.1177/14680874221112564.
[27] D.J. Hautman, F.L. Dryer, K.P. Schug, I. Glassman, A multiple-step overall kinetic mechanism for the oxidation of hydrocarbons, Combust. Sci. Technol. 25 (5–6) (1981) 219–235, https://doi.org/10.1080/00102208108547504.
[28] H. Wang, M. Yao, Z. Yue, M. Jia, R.D. Reitz, A reduced toluene reference fuel chemical kinetic mechanism for combustion and polycyclic-aromatic hydrocarbon predictions, Combust Flame 162 (6) (2015) 2390–2404, https://doi.org/10.1016/j.combustflame.2015.02.005.
[29] R.D. Reitz, Modeling atomization processes in high-pressure vaporizing sprays, Spray Technol. 3 (1987) 309–337.
[30] N.G. Rosa P. Villedieu J. Dewitte G. Lavergne A New Droplet-Wall Interaction Model, in 10th International Conference on Liquid Atomization and Spray Systems (ICLASS-2006) Kyoto Japan.
[31] C. Bai A.D. Gosman, Development of Methodology for Spray Impingement Simulation, Feb. 1995. https://doi.org/10.4271/950283.
[32] M.A. Lopez de Bertodano, C.-S. Jan, S.G. Beus, Annular flow entrainment rate experiment in a small vertical pipe, Nucl. Eng. Des. 178 (1) (1997) 61–70, https://doi.org/10.1016/S0029-5493(97)00175-1.
[33] S. Gepperth, Experimentelle Untersuchung Des Primarzerfalls an Generischen Luftgestutzten Zerstaubern Unter Hochdruckbedingungen, Vol. 75, Logos Verlag Berlin GmbH, Berlin, Germany, 2019.
[34] S. Gepperth, A. Müller, R. Koch, H.J. Bauer, Ligament and droplet characteristics in prefilming airblast atomization, in: ICLASS, 12th Triennial International Annual Conference on Liquid Atomization and Spray Systems, 2012, pp. 1–8.
[35] A.H. Govan, Modelling of vertical annular and dispersed two-phase flows, Imperial College London (University of London), 1990.
[36] H. Yamashita, M. Shimada, T. Takeno, A numerical study on flame stability at the transition point of jet diffusion flames, in: Symposium (international) on combustion, Vol. 26, No. 1, Elsevier, 1996, pp. 27–34, https://doi.org/10.1016/S0082-0784(96)80196-2.
[37] O. Colin, A. Benkenida, The 3-zones extended coherent flame model (Ecfm3z) for computing premixed/diffusion combustion, Oil Gas Sci. Technol. 59 (6) (2004) 593–609, https://doi.org/10.2516/ogst:2004043.
[38] B. Cuenot, T. Poinsot, Effects of curvature and unsteadiness in diffusion flames. Implications for turbulent diffusion combustion, in: Symposium (International) on Combustion, Vol. 25, No. 1, Elsevier, 1994, pp. 1383–1390, https://doi.org/10.1016/S0082-0784(06)80781-2.
[39] T. Poinsot, D. Veynante, Theoretical and Numerical Combustion, RT Edwards, Inc., 2005.
[40] A. d'Adamo, C. Iacovano, S. Fontanesi, A data-driven methodology for the simulation of turbulent flame speed across engine-relevant combustion regimes, Energies (Basel) 14 (14) (2021) 4210, https://doi.org/10.3390/en14144210.
[41] J. Kim, R. Scarcelli, S. Som, A. Shah, M.S. Biruduganti, D.E. Longman, Assessment of turbulent combustion models for simulating prechamber ignition in a natural gas engine, J. Eng. Gas Turbine Power 143 (9) (2021), https://doi.org/10.1115/1.4050482.
[42] C. Iacovano, A. D'Adamo, G. Cantore, Analysis and simulation of non-flamelet turbulent combustion in a research optical engine, Energy Procedia 148 (2018) 463–470, https://doi.org/10.1016/J.EGYPRO.2018.08.121.
[43] X. Sun, X. Liang, G. Shu, Y. Wang, Y. Wang, H. Yu, Effect of different combustion models and alternative fuels on two-stroke marine diesel engine performance, Appl. Therm. Eng. 115 (2017) 597–606, https://doi.org/10.1016/j.applthermaleng.2016.12.093.
[44] N.M. Hafiz, M.R.A. Mansor, W.M.F. Wan Mahmood, Simulation of the combustion process for a CI hydrogen engine in an argon-oxygen atmosphere, Int J Hydrogen Energy 43 (24) (2018) 11286–11297, https://doi.org/10.1016/J.IJHYDENE.2018.05.022.
[45] H. Zhu, Y. Zhang, F. Liu, W. Wei, Effect of excess hydrogen on hydrogen fueled internal combustion engine under full load, Int. J. Hydrogen Energy 45 (39) (2020) 20419–20425, https://doi.org/10.1016/J.IJHYDENE.2019.12.022.
[46] Y. An, M. Jaasim, V. Raman, F.E.H. Pérez, J. Sim, J. Chang, H.G. Im, B. Johansson, Homogeneous charge compression ignition (HCCI) and partially premixed combustion (PPC) in compression ignition engine with low octane gasoline, Energy 158 (2018) 181–191, https://doi.org/10.1016/J.ENERGY.2018.06.057.
[47] Y. Peial, et al., CFD-Guided Heavy Duty Mixing-Controlled Combustion System Optimization with a Gasoline-Like Fuel, SAE Int. J. Commer. Veh. 10 (2017-01–0550) (2017) 532–546, https://doi.org/10.4271/2017-01-0550.
[48] S.D. Givler, M. Raju, E. Pomraning, P.K. Senecal, N. Salman, R. Reese, Gasoline Combustion Modeling of Direct and Port-Fuel Injected Engines using a Reduced Chemical Mechanism, 2013. https://doi.org/10.4271/2013-01-1098.
[49] R. Scarcelli, J. Sevik, T. Wallner, K. Richards, E. Pomraning, P.K. Senecal, Capturing cyclic variability in EGR dilute SI combustion using multi-cycle rans, Am. Soc. Mech. Eng. (2015), https://doi.org/10.1115/ICEF2015-1045.
[50] W.N.W. Mansor, D.B. Olsen, Computational modeling of diesel and dual fuel combustion using CONVERGE CFD software, ARPN J. Eng. Appl. Sci. (2016).
[51] M. Battistoni, F. Mariani, F. Risi, C. Poggiani, Combustion CFD modeling of a spark ignited optical access engine fueled with gasoline and ethanol, Energy Procedia 82 (2015) 424–431, https://doi.org/10.1016/J.EGYPRO.2015.11.829.
[52] A.C. Ravindran, S.L. Kokjohn, The challenges of using detailed chemistry model for simulating direct injection spark ignition engine combustion during cold-start, Int. J. Engine Res. 24 (1) (2023) 161–177, https://doi.org/10.1177/14680874211045968.